Scattering bottleneck for spin dynamics in metallic helical antiferromagnetic dysprosium

M. C. Langner,[1] S. Roy,[2] A. F. Kemper,[3] Y.-D. Chuang,[2] S. K. Mishra,[2] R. B. Versteeg,[2] Y. Zhu,[1] M. P. Hertlein,[2] T. E. Glover,[2] K. Dumesnil,[4] and R. W. Schoenlein[1]

[1]*Materials Science Division, Lawrence Berkeley National Laboratory, Berkeley, California 94720, USA*
[2]*Advanced Light Source, Lawrence Berkeley National Laboratory, Berkeley, California 94720, USA*
[3]*Computational Sciences Division, Lawrence Berkeley National Laboratory, Berkeley, California 94720, USA*
[4]*Institut Jean Lamour (UMR CNRS 7198), Université de Lorraine, Vandoeuvre les Nancy F-54500, France*

(Received 11 September 2014; revised manuscript received 14 October 2015; published 23 November 2015)

Ultrafast studies of magnetization dynamics have revealed fundamental processes that govern spin dynamics, and the emergence of time-resolved x-ray techniques has extended these studies to long-range spin structures that result from interactions with competing symmetries. By combining time-resolved resonant x-ray scattering and ultrafast magneto-optical Kerr studies, we show that the dynamics of the core spins in the helical magnetic structure occur on much longer time scales than the excitation of conduction electrons in the lanthanide metal Dy. The observed spin behavior differs markedly from that observed in the ferromagnetic phase of other lanthanide metals or transition metals and is strongly dependent on temperature and excitation fluence. This unique behavior results from coupling of the real-space helical spin structure to the shape of the conduction electron Fermi surface in momentum space, which creates a bottleneck in spin scattering events that transfer the valence excitation to the core spins. The dependence of the dynamics on the intersite interactions renders the helical ordering much more robust to perturbations than simple ferromagnetic or antiferromagnetic ordering, where dynamics are driven primarily by on-site interactions.

DOI: 10.1103/PhysRevB.92.184423 PACS number(s): 71.20.Eh, 78.70.Ck

I. INTRODUCTION

The magnetic ground state of a material system is governed by the energetics of different spin and charge coupling such as exchange, dipolar, and spin-orbit interactions. Preferential destabilization of any one of the interactions can have profound effects on the net magnetic properties of the material. One way to manipulate the magnetic state is by applying external magnetic fields, which is often exploited in storage technologies to write information. With decreasing bit sizes and higher storage density, the long-range switching fields are no longer favorable. A new paradigm is to use a controlled impulse to change the magnetization. An example of such an impulse is the strong electric field created by a femtosecond laser pulse. Intense research efforts seek to understand how fast and by what mechanism magnetic order is reestablished after a femtosecond impulse destroys the long-range order [1]. In particular, as the time scale of the perturbation approaches the characteristic time of the exchange interaction (10–100 fs), the magnetic dynamics may enter a novel coupling regime where new exchange pathways may be established [2,3]. These questions become increasingly complex in antiferromagnets where after the exchange is destabilized, a competition may arise between the inter- and intrasublattice ordering. Thus there may exist more than one pathway to establish the ground state and as a result, new transient phases may be observed.

Ultrafast optical measurements have been used to explore fundamental spin-scattering mechanisms and control the magnetic state on femtosecond time scales in systems with spatially uniform magnetic phases [1]. The advent of time-resolved x-ray scattering techniques has opened the door for similar studies in longer-range magnetic structures that result from magnetic interactions with competing symmetries. Lanthanide metals exhibit a variety of magnetic phases due to competition between spin-orbit coupling, magnetoelastic effects, and long-range exchange coupling mediated by the indirect RKKY (Ruderman-Kittel-Kasuya-Yoshida) interaction [4]. The nature of the exchange interaction creates a composite spin system composed of closely coupled conduction and core electron spins that account for the majority of the magnetic moment. Helical or conically ordered phases, where the magnetic structure is characterized by a nonzero ordering wave vector, are created by competing symmetric and antisymmetric long-range exchange interactions, where the exchange interactions are determined by the spatial distribution of the conducting electron wave functions.

Ultrafast demagnetization mechanisms have been previously explored in transition metal and lanthanide magnets using all-optical and x-ray dichroism techniques [1,5–8]. These studies have focused on the angular momentum transfer between core spins, conducting spins, and lattice, and addressed the dynamics of the uniform ferromagnetic phase. Ultrafast optical pump/x-ray probe measurements reveal the coupling mechanisms between the constituent spin systems in lanthanide magnets by observing the dynamics of core spins in response to excitation of conduction electrons responsible for the exchange interaction. An as yet unexplored aspect of these magnetic systems is the dynamics in the helical phase, where transiently altering the conduction electron distribution can have a profound influence on the long-range magnetic structure.

In this study, we measure the dynamics of the inner-shell f-electron spin helix in dysprosium in response to transient injection of conduction electrons with unpolarized spins. We observe a reduction in the amplitude of the helical order parameter and a shift in the helical wave vector q on disparate time scales that are strongly dependent on both pump fluence and sample temperature. Measurements of the ferromagnetic (FM) phase dynamics is consistent with FM phase measurements of lanthanide metals such as Tb and

Gd, where the dynamics of the core and conducting spins occur on ps time scales [5,6,8]. Notably, the dynamics in the helical antiferromagnetic phase (HAF) of Dy are significantly slower, with characteristic time scales of tens of picoseconds. We attribute these anomalous dynamics to the relationship between the wave vector of the conduction level electronic excitation k and the wave vector of the core magnetic ordering q. In the FM phase, the electronic excitation at $k = 0$ is closely coupled to the magnetic ordering at $q = 0$. In the HAF phase, the core-spin helix is concomitant with a nesting of the Fermi surface (FS). Initial ultrafast scattering of spins from the $k = 0$ excitation does not directly change the energy-minimizing configuration of the system, and instead the helical dynamics are driven by changes to the shape of the FS and subsequent changes to the electron distribution through scattering events.

Magnetization dynamics were investigated in an epitaxially grown yttrium/dysprosium/yttrium (20/500/20 nm) multilayer film that exhibits a second-order phase transition to a helical antiferromagnetic phase below $T_N = 180$ K [9]. A magnetostriction-driven first-order transition to a ferromagnetic phase occurs at $T_C = 60$ K, where T_C is reduced relative to the bulk due to strain induced by the underlying yttrium layer. Between T_N and T_C, the pitch of the spin helix, $\theta = qa$ (where a is the lattice constant), changes continuously with temperature, from 46° ($q = 2.24$ nm^{-1}) at T_N to 30° ($q = 1.46$ nm^{-1}) at T_C [10].

II. EXPERIMENTAL RESULTS

A. Ultrafast optical measurements

Dynamics of the low-temperature FM phase were observed using magneto-optical Kerr measurements. The photoinduced change in reflectivity (dR/R) and magneto-optic Kerr (MOKE) angle ($d\theta$) for the Y/Dy/Y stack are shown in Fig. 1. The reflectivity and MOKE measurements were recorded using 100 fs pulses with a probe energy of 3.0 eV and an excitation energy of 1.5 eV. These measurements were performed in a polar geometry with an applied field of 0.5 T perpendicular to the sample surface. The reflectivity signal shows multiple-time-scale dynamics within 2 ps, which we attribute to reflections from the front surface and the top Y/Dy interface. The $d\theta$ dynamics show a rise time of ∼300 fs. Both signals show a recovery time of 2.5 ps and a remnant excitation beyond 10 ps.

The MOKE signal shows a clear change in amplitude at the ferromagnetic transition temperature. This change occurs within 1 ps, indicating that the 1.5 eV optical pulse excites the conduction-level magnetism on time scales similar to those observed in previous ultrafast measurements of lanthanide magnets [1,5–8]. A sharp change in amplitude at T_C is not observed in the reflectivity measurements. Dynamics of the MOKE signal continue above T_C in the AFM and paramagnetic phases, which we attribute to dynamics of the field-canted out-of-plane magnetic moment.

The 20 nm top Y layer absorbs ∼90% of the pump energy, creating a hot electron distribution in the Y layer and resulting in ultrafast injection of unpolarized spins into the 500 nm Dy film via nonequilibrium diffusion [5,6,11]. The MOKE measurements indicate an ultrafast excitation of

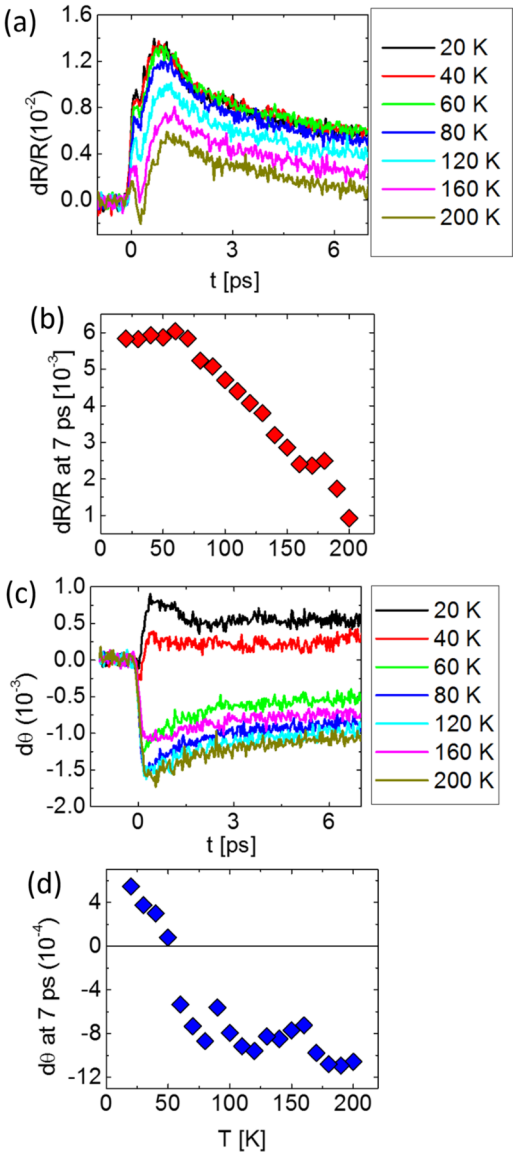

FIG. 1. (Color online) Optical pump-probe data of the Y/Dy/Y thin film. (a) dR/R as a function of temperature from 20 K (top, purple) to 200 K (bottom, black). (b) Temperature dependence of the dR/R amplitude. (c) $d\theta_K$ as a function of temperature from 20 K (top, purple) to 200 K (bottom, black). (d) Temperature dependence of the amplitude of $d\theta_K$.

the conduction level spins, resulting from sub-ps injection of hot unpolarized electrons from the Y layer and consistent with dynamics observed for the same process in other magnetic materials [5,6,11].

B. Resonant scattering measurements

Dynamics in the helical phase were probed using resonant x-ray scattering, which provides a direct probe of the core-spin helical ordering through direct optical transitions between atomic core levels and the valence f orbital [10]. As in the MOKE measurements, the sample is excited with an optical pump pulse with a photon energy of 1.5 eV and a duration of 100 fs. Time-resolved diffraction measurements

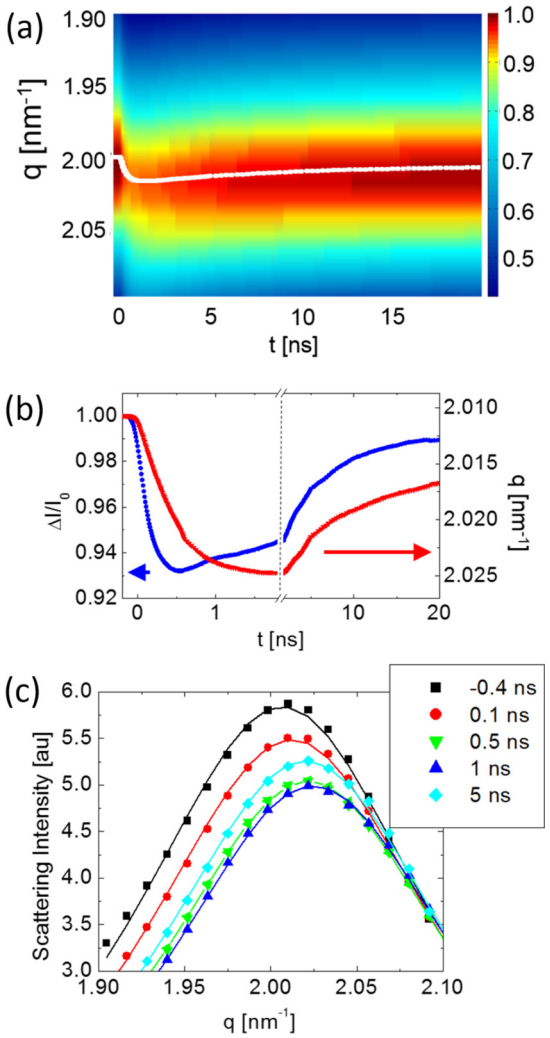

FIG. 2. (Color online) (a) Color map of the diffraction peak intensity as a function of time delay, recorded by scanning time delay at different scattering wave vectors. The white line indicates the time dependence of the scattering wave vector. (b) Scattering peak intensity (blue curve, left axis) and wave vector (red curve, right axis) as a function of time delay for data in panel (a). Note that the axis of the wave vector in (a) and (b) has been inverted to accommodate comparison of the I and q dynamics. (c) Rocking curve scans at different time delays. Solid lines represent fits with fixed rocking curve width.

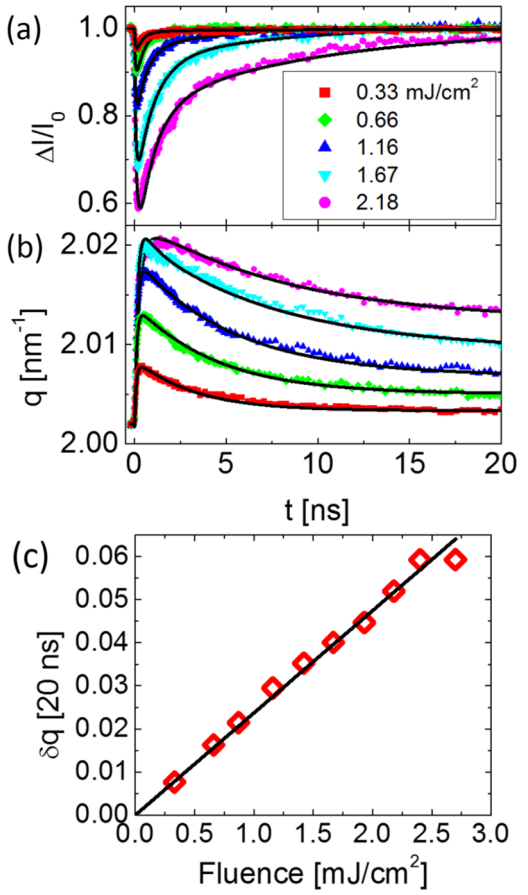

FIG. 3. (Color online) Time dependence of the loss in diffraction peak intensity (a) and change in q vector (b) as a function of pump fluence. Solid lines indicate fits to the model described in the text. (c) Remnant change in q as a function of pump fluence showing linear dependence consistent with sample heating.

were performed at beamline 6.0.2 at the Advanced Light Source, Lawrence Berkeley National Laboratory, utilizing a probe energy of 1290 eV, resonant with the Dy M5 edge, with a probe pulse duration of 70 ps.

Figure 2 shows the spiral diffraction peak with a pump fluence of 0.66 mJ/cm^2 at 105 K as a function of pump-probe time delay. The dynamics of the diffraction peak, consisting of the onset of the excitation and subsequent recovery, are faster than the corresponding shifts in scattering wave vector. The initial response of the helix is characterized by a reduction of diffraction intensity (I) occurring on a 200 ps time scale, and an increase of the peak wave vector (q) occurring on a 1 ns time scale. Both q and I recover on time scales of several ns. The parameters I and q are determined by fitting the measured rocking curve with a Lorenztian function. The diffraction peak corresponds to the periodicity of the helix perpendicular to the plane of the film, and we observe no change in the rocking curve width within the accuracy of the fits ($\sim$2%), which is likely limited by the 30 nm penetration depth of the x-ray probe. There is also no observable change in the diffraction peak width that would indicate a change in the in-plane domain structure, and the dynamics of the diffraction signal can therefore be completely characterized by $I(t)$ and $q(t)$.

Figure 3 shows the time dependence of I and q as a function of pump fluence at 105 K. The excitation and recovery dynamics become slower with increased fluence for both the parameters. The maximum reduction in the diffraction intensity ($\delta I/I_0$) is linear with fluence. The shift in wave vector shows a saturation-like behavior at early time delays with fluences above 1.5 mJ/cm^2 and is linear with fluence for delays $>$20 ns. The slow dynamics of the core-spin spiral is in stark contrast with the ultrafast MOKE measurements of the conduction-level magnetism.

On long time scales ($>$20 ns), the changes in the diffraction peak are consistent with a uniform increase in the sample temperature. As the sample is cooled from T_N to T_C,

static measurements show a monotonic decrease in q with little variation in the diffraction efficiency at intermediate temperatures [10]. Thus on a 20 ns time scale both I and q can be parametrized by an increase in the sample temperature T, such that the magnetic state described by $I(T)$,$q(T)$ maps onto measured static values. The increase in q vector with fluence is shown in Fig. 3(c) at 105 K. The linear dependence on fluence is expected for a regime in which the specific heat is roughly constant with photoinduced change in temperature: $dT = dE/C(T) \sim dE/C$, where C is the specific heat and dE is the energy deposited by the pump pulse. The maximum temperature increase is ∼5 K at the highest fluence. Thermal lattice changes can also be eliminated as the cause of the time-dependent shift in q. The lattice constant along the spiral direction is reduced by $\delta c/c = 0.003$ as the sample is heated through the helical phase, making the observed shifts in the magnetic wave vector q with laser excitation too large to be attributed to a thermal change in the lattice constant [9].

At times shorter than ∼20 ns, the large transient photoinduced reduction in I, coupled with only a moderate increase in q, is not consistent with any statically measured magnetic configuration, and indicates that the dynamics observed on time scales faster than ∼20 ns cannot be described by an increase in the sample temperature. Specifically, by comparing the time-resolved data with static temperature-dependent measurements of the rocking curve, the shape of the rocking curve cannot be characterized by $I(T)$, $q(T)$, and a time-dependent temperature at these time scales. The spiral wave vector remains uniform throughout the probed region, as indicated by the constant rocking curve width, and indicates that spatial inhomogeneities in the excitation region are not responsible for the observed changes in the diffraction peak.

Figure 4 shows the temperature dependence of the spin-ordering peak dynamics. Both the onset and recovery of the q shift become progressively slower with increasing temperature. The dynamics of $\delta I/I$ show a less dramatic slowing with temperature. The maximum shift in q is nonmonotonic with temperature, with a maximum shift at 90 K. The photoinduced reduction in I shows little dependence on temperature, except near T_N, as shown in Fig. 4.

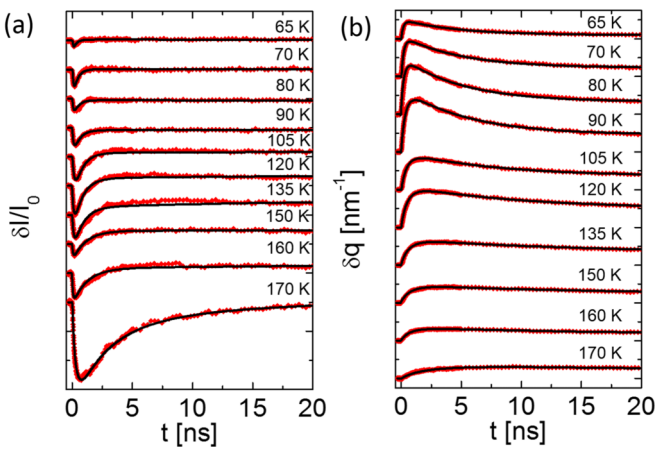

FIG. 4. (Color online) Temperature dependence of (a) $\delta I/I$ and (b) wave vector (q) for a pump fluence of 0.66 mJ/cm^2. Lines are fits from the GP model described in the text.

III. DISCUSSION

The microscopic origin of the HAF dynamics is clarified by considering the relationship between the core-spin ordering and the conduction electron FS. In equilibrium, the FS has extended regions in which electrons can scatter from $\phi(k)$ to $\phi(k+q)$, which combined with the exchange interaction between core and conduction spins leads to helical ordering of the core spins with wave vector q [12]. The temperature dependence of q results primarily from the dependence of the helical ordering energy gap on thermal fluctuations of the basal plane magnetization, leading to a reshaping of the FS as the thermal fluctuations are frozen out [13–16].

In the spiral phase, the 1.5 eV excitation generates hot electrons, creating an excitation at $k = 0$ in the conduction spins and perturbing the conduction-level magnetic ordering while preserving the FS nesting q. The induced disorder of the conduction spins reduces the number of quasielastic $k \rightarrow k+q$ scattering events where spin angular momentum is conserved, and increases $k \rightarrow k+q$ scattering involving changes in angular momentum. The core/conduction exchange couples this angular momentum scattering to the core helix, propagating spin disorder to the core spins, but not initially changing the favored helical wave vector.

The response of the core spins to the perturbed conduction electron distribution mimics the reduction in the magnetization due to thermal excitations, and the equilibrium wave vector q for the FS nesting and core helix changes due to the dependence of q on the basal plane magnetization. This process is diagramed in Fig. 5. The shift in the nesting vector of the FS creates a mismatch between the FS and the electron distribution. The electron distribution relaxes via inelastic scattering events that couple electrons with excess energy (above E_{Fermi}) with hole states below E_{Fermi}, with transfer of spin angular momentum occurring through exchange and spin-orbit coupling interactions. This situation is analogous to the breathing Fermi surface model used to describe damping of the precession in ferromagnets, in which the dynamical pointing of the ferromagnetism alters the FS through spin-orbit coupling [17–19]. The excitation time scales observed in the helical system are similar to damping time scales in other magnetic systems, limited by the scattering rate and efficiency of angular momentum transfer during scattering events.

IV. MODEL

For nonthermal dynamics in magnetic systems, the three-temperature model (3 TM) is often invoked to describe the dynamics in terms of energy transferred between electronic, lattice, and spin degrees of freedom, with laser-induced disorder in the spin system modeled as an increase in spin temperature T_S [1,20,21]. In a ferromagnet, this spin temperature defines the state of a global, uniform magnetization. In the HAF phase of Dy, the magnetic state is defined by both the strength of the order parameter and the helical wave vector, and the electronic configuration and helical ordering are interdependent through nesting of the FS. A model with single effective spin temperature and the parametrization $I(T_S)$,$q(T_S)$ fails to describe the short-time-scale dynamics, as discussed above, as a single spin temperature cannot

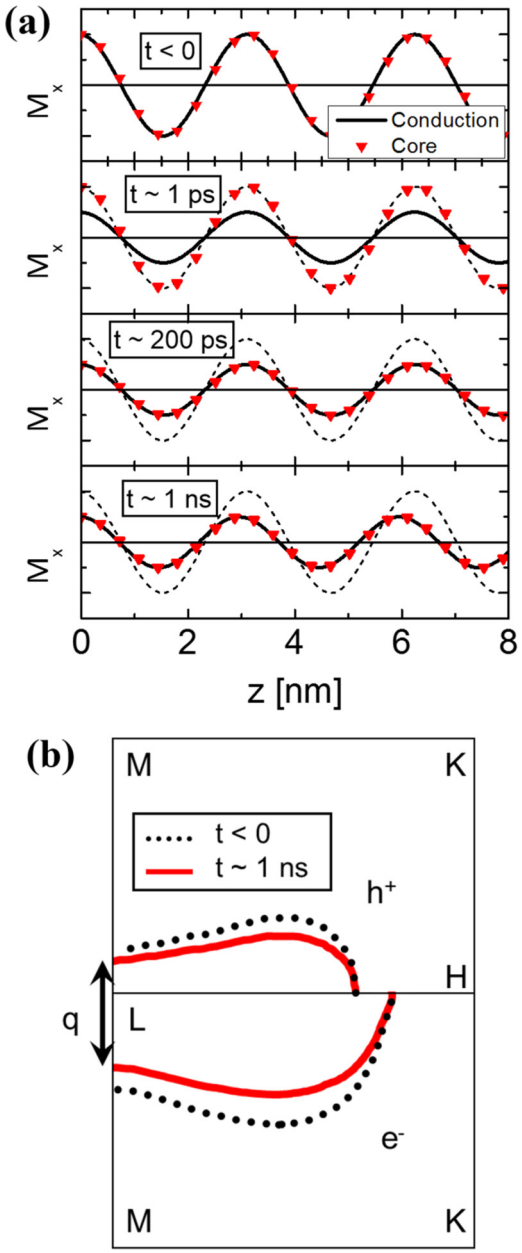

FIG. 5. (Color online) (a) Diagram of real-space spin ordering of core and conduction electrons for a spiral with $q \| z$. The y-axis units are arbitrary. $t < 0$: Equilibrium distribution. $t \sim 1$ ps: Photoexcitation of conduction electrons, followed by ($t \sim 200$ ps) excitation of core spins and ($t \sim 1$ ns) subsequent shift in q. The dotted lines show the equilibrium distribution for reference. (b) Corresponding FS diagram. Adapted from Ref. [12].

account for both parameters of the magnetic configuration. While the 3 TM includes a phenomenological treatment of the core spin/conduction electron coupling, it does not naturally account for the effect of this coupling on the shape of the FS and the closely related helical spin configuration.

Instead, we employ a Gross-Pitaevskii (GP) model, which models the dynamics through motion of a free energy surface, phenomenologically accounting for both the coupled magnetic state parameters I and q and changes to the shape of FS [22,23]. We use this model to derive changes to the exchange constants which are consistent with the ultrafast dynamics measured in Fig. 2. We use a Hamiltonian given by

$$H = \frac{J_1}{2a}\int d^3x\left[-\frac{\theta}{2}(\nabla m)^2 + \frac{a}{4}\left(\nabla^2 m\right)^2\right], \qquad (1)$$

where m is the strength of the order parameter of the HAF, proportional to the experimentally measured I. This Hamiltonian contains the exchange terms J_1 and J_2, which are the effective nearest and next-nearest neighbor coupling between core spins that stabilize the helical phase. J_2 appears through θ, which is the equilibrium turn angle of the helix given by $\cos(\theta) = J_1/4J_2$. The helix is the lowest energy state of this system when J_1 and J_2 have opposite sign.

For a one-dimensional helical magnetic structure with wave vector q, the above Hamiltonian leads to an effective free energy given by

$$F = -m^2\alpha(T) + \beta m^4 + \frac{1}{2}J_1 a^2 m^2\left(-\frac{\theta^2 q^2}{2} + \frac{a^2 q^4}{4}\right). \qquad (2)$$

The first two terms, with factors α and β, are the lowest-order terms in the free energy expansion that stabilize the order parameter for $T < T_N$, and a is the lattice constant. Changes to the free energy of the core helix arising from excitation of the conduction electrons are considered through the parameters J_1 and J_2. Note that θ and q are retained as variables to distinguish the equilibrium helix turn angle from the measured dynamic variable q.

The dynamics can be calculated by using the Hamiltonian to describe an effective action of the helical system parameterized by m and q. From Eq. (2), we can write the equations of motion as

$$\gamma_m \dot{m} = 2\alpha m - 4\beta m^3 - J_1 m a^2\left(-\frac{q^2\theta^2}{2} + \frac{a^2 q^4}{4}\right), \qquad (3)$$

$$\gamma_q \dot{q} = -\tfrac{1}{2}J_1 m^2 a^2 q(-\theta^2 + a^2 q^2). \qquad (4)$$

Due to the absence of oscillations in the data, we neglect the second derivative terms in the above equation. Additionally, we have introduced phenomenological damping terms with parameters γ_m and γ_q to account for relaxation of the system back to equilibrium.

The behavior of m and q with different rheonomic constraints provides insight into the origins of the dynamics of the spin helix. Within the GP model, the dynamics of the parameters $J_{1,2}$ emulate the dynamics of the FS, and the damping parameters model the scattering mechanisms that drive the spin-ordering to match the FS. The observed dynamics I and q are described by introducing time-dependent parameters $J_1(t)$ and $J_2(t)$ into Eqs. (3) and (4) such that the derived m and q match the data.

We choose $J_1(t)$ and $J_2(t)$ to be consistent with our microscopic picture in the following ways. The uniform ($k = 0$) excitation of the conduction electrons is modeled as a proportional reduction in both exchange parameters, such that initially the equilibrium q vector is unchanged. We introduce two recovery time constants to describe the observed recovery times in the data, and we introduce parameters σ and ρ_2 to account for the symmetric and asymmetric recovery amplitudes of the exchange constants. Within this model, the

exchange parameters vary according to

$$\frac{\delta J_1(t)}{J_1(0)} = \delta J_{\text{init}}[(1-\sigma-\delta J_{T,1})e^{-t/\tau_a} + \sigma e^{-t/\tau_b} + \delta J_{T,1}], \tag{5}$$

$$\frac{\delta J_2(t)}{J_2(0)} = \delta J_{\text{init}}[(1-\sigma-\rho_2)e^{-t/\tau_a} + \sigma e^{-t/\tau_b} + \rho_2 e^{-t/\tau_2}]. \tag{6}$$

The onset of the reduction in $J_{1,2}$ is instantaneous to be consistent with observed optical MOKE data in Fig. 1, and the slow onset of the reduction in m is limited by the damping parameter γ_m. Shifts in q are treated as partial asymmetric recoveries of either exchange parameter. The black lines in Fig. 3 show fits to the data using $m(t)$ and $q(t)$ calculated with the GP model.

Figure 6(a) shows the initial reduction in the exchange parameters δJ_{init} and the recovery amplitude σ. The initial reduction in the exchange is linear with fluence, as would be expected from an effective exchange proportional to the spin ordering and an injected unpolarized spin population that scales with the fluence. The initial changes in the exchange constants are equal for J_1 and J_2 and therefore do not lead to a shift in the spiral wave vector. The time scales for the recovery, τ_a and τ_b, are shown in Fig. 6(b).

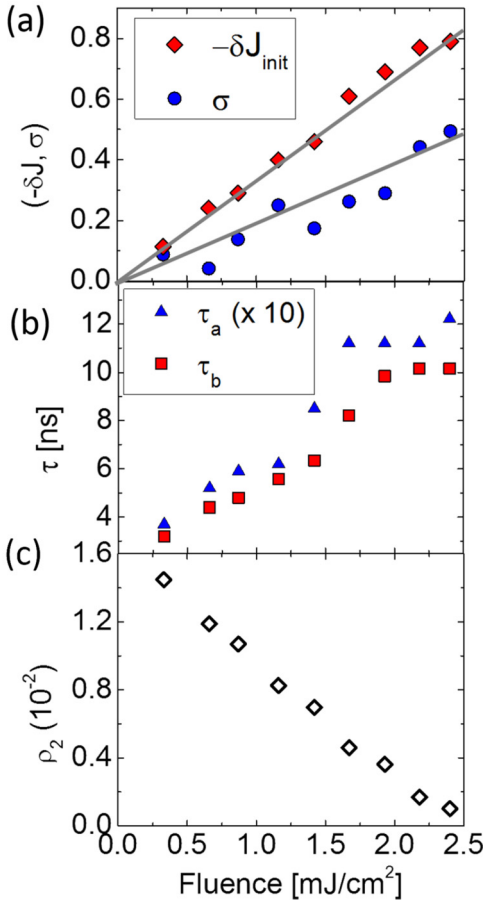

FIG. 6. (Color online) Magnitudes and time scales of changes in exchange parameters J_1 and J_2 used to describe the fluence dependence of the data. (a) Amplitudes of initial reduction and proportional recovery of the exchange parameters. Note that δJ_{init} is negative, and the line indicates a linear reduction in the exchange parameters with fluence. (b) Proportional recovery time scales. (c) Nonproportional recovery in J_2 leading to the shift in q. ρ_2 becomes smaller with fluence, leading to saturation-like behavior for the shift in spiral wave vector.

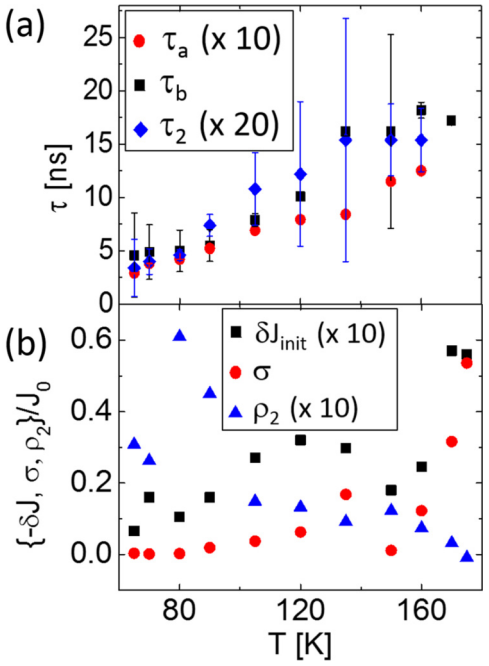

FIG. 7. (Color online) (a) Time scales of exchange parameters J_1 and J_2 as a function of temperature. (b) Reduction amplitudes of J_1 and J_2 as a function of temperature.

The initial shift in q occurs through a relatively fast recovery of J_2 through the term ρ_2. This parameter is shown in Fig. 6(c). The shift in q for time delays greater than 20 ns is treated through $J_{T,1}$, which is a small remnant reduction in J_1 representing an increased sample temperature. Note that $\{J_{T,1}, \rho_2\} \ll \{\delta Ji, \sigma\}$; the terms representing antisymmetric dynamics in J_1 and J_2 that shift the spiral q are much smaller than the symmetric changes in the exchange constants, resulting in overall dynamics of J_1 and J_2 that are nearly symmetric.

The modeled time constants become slower with increasing fluence [Fig. 6(b)] and also become slower as T is increased from T_C to T_N as shown in Fig. 7(a). Both of these trends suggest a link between the magnetic ordering and the recovery time scales of the spin helix. Figure 7(b) shows the temperature-dependent changes in J_1 and J_2, with increases in the symmetric parameters near T_N corresponding to softening of $J_1(0), J_2(0)$ near the transition temperature. The combined fluence and temperature dependence of the time constants is consistent with changes in the shape of the FS, with a corresponding reduction in the effective exchange coupling between core spins, resulting from a reduction of the basal plane magnetization m [13–16].

Moreover, the GP model adequately describes the $\delta I/I$ temperature dependence in Fig. 4(a), which shows an increase in scattering signal on time scales of ∼10 ns for intermediate

temperatures. This results from the relatively slow damping of the spiral wave vector to the pseudoequlibrium excited value and a relatively large change in θ relative to the change in J_1. From (2), the equilibrium m is related to q and θ by

$$m_0 = \sqrt{\frac{J_1 a^2 q^2 \left(2\theta^2 - a^2 q^2\right) + 8\alpha}{16\beta^2}}. \quad (7)$$

The equilibrium turn angle θ is increased by the laser excitation, which leads to a larger difference θ and aq and an increase in m_0. This increase will appear in the dynamic parameter m whenever J_1 and θ reach pseudoequilibrium excited values and m damps quickly relative to the damping time of q.

The equilibrium helical phase results from the interaction between the core spins and the nested FS of the conduction electrons; the phenomenological GP model provides a shorthand to account for dynamics of the nested FS through $J_{1,2}$ and subsequent electron population scattering events through $\gamma_{m,q}$. By considering changes to the shape of the free energy surface, the GP model provides an accurate description of the helical motion with fluence and temperature dependence that is qualitatively consistent with both the static and optical dynamic measurements. We observe a linear reduction in the exchange coupling with laser fluence, indicating a direct excitation of the conduction electrons, and fluence and temperature dependence of the recovery time scales consistent with an effective exchange coupling that scales with m.

In summary, the dynamics of the helical phase in response to transient unpolarized spin injection differ significantly from those in the ferromagnetic phase due to the relationship between the core spins and conduction electron FS nesting. FM phase dynamics result from close coupling of the $k = 0$ excitation to the core spins through spin-orbit coupling and short-range exchange interactions. The dynamics of the helical phase result from indirect excitation to the finite wave-vector ordering through a fundamentally different process, analogous to a damping mechanism, that transfers angular momentum between the excited conduction electrons and core spins.

ACKNOWLEDGMENTS

The work at LBNL, including experiments at ALS, was supported by the Director, Office of Science, Office of Basic Energy Sciences, of the US Department of Energy under Contract No. DEAC02-05CH11231.

[1] A. Kirilyuk, A. V. Kimel, and T. Rasing, Rev. Mod. Phys. **82**, 2731 (2010).
[2] S. Mathias, C. La-O-Vorakiat, P. Grychtol, P. Granitzka, E. Turgut, J. M. Shaw, R. Adam, H. T. Nembach, M. E. Siemens, S. Eich, C. M. Schneider, T. J. Silva, M. Aeschlimann, M. M. Murnane, and H. C. Kapteyn, Proc. Natl. Acad. Sci. USA **109**, 4792 (2012).
[3] I. Radu, K. Vahaplar, C. Stamm, T. Kachel, N. Pontius, H. A. Dürr, T. Ostler, J. Barker, R. Evans, R. Chantrell, A. Tsukamoto, A. Itoh, A. Kirilyuk, T. Rasing, and A. Kimel, Nature (London) **472**, 205 (2011).
[4] B. Coqblin, *The Electronic Structure of Rare Earth Metals and Alloys* (Academic Press, New York, 1978).
[5] M. Wietstruk, A. Melnikov, C. Stamm, T. Kachel, N. Pontius, M. Sultan, C. Gahl, M. Weinelt, H. A. Dürr, and U. Bovensiepen, Phys. Rev. Lett. **106**, 127401 (2011).
[6] R. Carley, K. Döbrich, B. Frietsch, C. Gahl, M. Teichmann, O. Schwarzkopf, P. Wernet, and M. Weinelt, Phys. Rev. Lett. **109**, 057401 (2012).
[7] M. Lisowski, P. A. Loukakos, A. Melnikov, I. Radu, L. Ungureanu, M. Wolf, and U. Bovensiepen, Phys. Rev. Lett. **95**, 137402 (2005).
[8] A. Eschenlohr, M. Sultan, A. Melnikov, N. Bergeard, J. Wieczorek, T. Kachel, C. Stamm, and U. Bovensiepen, Phys. Rev. B **89**, 214423 (2014).
[9] K. Dumesnil, A. Stunault, P. Mangin, C. Vettier, D. Wermeille, N. Bernhoeft, S. Langridge, C. Dufour, and G. Marchal, Phys. Rev. B **58**, 3172 (1998).
[10] S.-W. Chen, H. Guo, K. A. Seu, K. Dumesnil, S. Roy, and S. K. Sinha, Phys. Rev. Lett. **110**, 217201 (2013).
[11] M. Battiato, K. Carva, and P. M. Oppeneer, Phys. Rev. Lett. **105**, 027203 (2010).
[12] S. C. Keeton and T. L. Loucks, Phys. Rev. **168**, 672 (1968).
[13] R. Elliott and F. Wedgwood, Proc. Phys. Soc. **81**, 846 (1963).
[14] R. Elliott and F. Wedgwood, Proc. Phys. Soc. **84**, 63 (1964).
[15] K. Yosida and A. Watabe, Prog. Theor. Phys. **28**, 361 (1962).
[16] K. M. Döbrich, A. Bostwick, J. L. McChesney, K. Rossnagel, E. Rotenberg, and G. Kaindl, Phys. Rev. Lett. **104**, 246401 (2010).
[17] V. Kamberský, Can. J. Phys. **48**, 2906 (1970).
[18] M. Fähnle and D. Steiauf, Phys. Rev. B **73**, 184427 (2006).
[19] D. Steiauf, J. Seib, and M. Fähnle, Phys. Rev. B **78**, 020410 (2008).
[20] T. Ogasawara, K. Ohgushi, Y. Tomioka, K. S. Takahashi, H. Okamoto, M. Kawasaki, and Y. Tokura, Phys. Rev. Lett. **94**, 087202 (2005).
[21] B. Koopemans, G. Malinowski, F. Dalla Longa, D. Steiauf, M. Fähnle, T. Roth, M. Cinchetti, and M. Aeschlimann, Nat. Mater. **9**, 259 (2010).
[22] F. Li, T. Nattermann, and V. L. Pokrovsky, Phys. Rev. Lett. **108**, 107203 (2012).
[23] E. Gross, Nuevo Cimento **20**, 454 (1961).